

# Efficient Thermal- and Photocatalyst of Pd Nanoparticles on TiO<sub>2</sub> Achieved by an Oxygen Vacancies Promoted Synthesis Strategy

Xiaoyang Pan<sup>†,‡</sup> and Yi-Jun Xu<sup>\*,†,‡</sup>

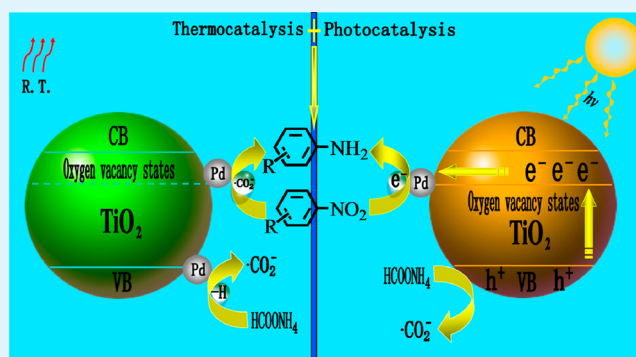
<sup>†</sup>State Key Laboratory of Photocatalysis on Energy and Environment, College of Chemistry and Chemical Engineering, Fuzhou University, Fuzhou, 350002, People's Republic of China

<sup>‡</sup>College of Chemistry and Chemical Engineering, New Campus, Fuzhou University, Fuzhou, 350108, People's Republic of China

## S Supporting Information

**ABSTRACT:** Pd nanoparticles supported on defective TiO<sub>2</sub> with oxygen vacancies (TiO<sub>2</sub>-OV) have been prepared by an oxygen vacancies mediated reduction strategy. The resulting Pd–TiO<sub>2</sub>-OV catalyst with uniform Pd nanoparticles deposition demonstrates a remarkably thermocatalytic activity toward rapid, efficient reduction of nitroaromatics in water. The reaction proceeds efficiently using HCOONH<sub>4</sub> as a hydrogen source under ambient conditions. The controlled experiments show that the <sup>•</sup>CO<sub>2</sub><sup>−</sup> radicals produced by dehydrogenation of HCOONH<sub>4</sub> are the main active species for the selective nitro reduction. Moreover, defective TiO<sub>2</sub> nanostructures deposited with Pd nanoparticles, featuring excellent visible-light absorption via the creation of oxygen vacancies, can take advantage of the solar and thermal energy to drive catalytic reduction reactions more efficiently at room temperature. During this process, the oxygen vacancies and Pd nanoparticles play synergetic roles in the photoreduction of nitro compounds. Our work would be beneficial for implementation of a novel defect-mediated catalytic system in which solar light energy can be coupled with thermal energy to drive an energy efficient catalytic process.

**KEYWORDS:** oxygen vacancies, selective reduction, Pd nanoparticles, thermocatalyst, photocatalyst



## 1. INTRODUCTION

The hydrogenation of nitroaromatics to corresponding amines is an important organic transformation in industrial chemistry, because amines are valuable intermediates for the production of fine chemicals.<sup>1–6</sup> Conventional methods for nitro reduction not only involve environmentally harmful stoichiometric reducing agents, organic solvents and stringent conditions, such as high pressure and temperature but also produce a number of toxic wastes.<sup>7</sup> Catalytic hydrogenation of aromatic nitro compounds with water as an inexpensive and environmentally friendly solvent is therefore an ideal process to overcome these drawbacks.<sup>8–15</sup> Especially, the selective nitro hydrogenation under ambient conditions using renewable and clean energy source, i.e., solar light, is highly desirable for a green and sustainable chemistry.<sup>5,6,14–16</sup> Nevertheless, related works are mainly concerned about rhodium- and ruthenium-based homogenous systems,<sup>1,3,17</sup> which have the drawback of difficulty in product isolation as well as the requirement of organic bases in large excess. Although heterogeneous catalysis offers several advantages over their homogeneous counterparts with respect to recycling, recovery and minimization of undesired hazardous wastes,<sup>7,18</sup> the reduction of nitro compounds by heterogeneous catalysts often requires high pressures, temperatures and longer reaction times.<sup>1,3,18–20</sup>

Supported noble metal nanoparticles have long been recognized as efficient catalysts for a wide range of organic transformations because of their unique catalytic properties under mild conditions.<sup>20–22</sup> Despite the tremendous efforts on the noble metal catalyzed selective oxidation reactions for green and sustainable organic synthesis, relatively few catalytic systems based on noble metal nanoparticles catalysts have succeeded in selective reduction of nitro compounds.<sup>23</sup> The most effective systems make use of Au particles deposited on TiO<sub>2</sub><sup>4,19,20</sup> and Ag particles coated with CeO<sub>2</sub>.<sup>24</sup> Although a few catalytic systems based on noble metals are succeeded in nitro reduction at room temperature,<sup>4,25,26</sup> high temperature (>100 °C) and high H<sub>2</sub> pressure (>500 kPa) are often required for driving the catalytic nitro reduction.<sup>19,20,24</sup> Therefore, the search for a new facile, efficient and environmentally friendly process under milder conditions is desirable for a safe and clean synthesis of amines.

Notably, the activities of these noble metal particles depend strongly on the size of metal particles and nature of supported oxides.<sup>27–31</sup> It is demonstrated that the small noble metal nanoparticles give much higher intrinsic activities than that of

Received: November 2, 2013

Accepted: January 6, 2014

Published: January 6, 2014

larger ones.<sup>29,30</sup> In addition, for the nitro reduction, specific metal-support interactions could endow the metal particles with new physicochemical characteristics and thus enhance their catalytic activities, because the supported metal oxide can play a precise functional role, differing from its conventional task as a simple support.<sup>32–34</sup> It has been demonstrated that the defect sites, particular oxygen vacancies on the support, are of key importance for modifying the electronic properties and for the increased activity of the noble metal nanoparticles toward nitro reduction.<sup>28</sup>

For the synthesis of metal nanoparticles, colloidal chemistry provides various efficient strategies for synthesizing metal nanoparticles with well-defined particle size distribution, in which the metal particles are stabilized in solution by the specific surfactant or organic ligands.<sup>25,33,35,36</sup> These organic species ensure that the small sized nanoparticles cannot coalesce.<sup>37</sup> However, these species could impair catalytic performance of metal particles largely, because their can strongly interact with the surface of metal and hinder the access of reactant to the metal surface.<sup>33,38</sup> In addition, for applying noble metal catalysts (e.g., Au–Al<sub>2</sub>O<sub>3</sub>, Pd–C, Pd–MgO) in the field of thermocatalysis, it should be noted that the supported metal oxides often consist of photoinactive magnesia, carbon and alumina,<sup>7,12,31,39</sup> which cannot utilize the green and free solar light energy. Therefore, if the supported metal oxide can be photoexcited under visible light irradiation, it may offer a new possibility for the development of energy efficient catalytic processes with sunlight as the main energy source. Importantly, the photoactive metal oxide supported thermoactive noble metal nanoparticles may realize novel catalytic systems, in which thermal energy can be coupled with solar energy to drive a more energy efficient process for nitro reduction.

Herein, Pd nanoparticles are directly grown on the defective TiO<sub>2</sub> with oxygen vacancies (TiO<sub>2</sub>-OV), which utilizes neither reducing agents nor stabilizing molecules. Through the redox reaction between the Pd ions and reductive TiO<sub>2</sub>-OV, Pd nanoparticles with average particle size of ca. 2 nm are homogeneously distributed on the TiO<sub>2</sub>-OV matrix. The resulting Pd–TiO<sub>2</sub>-OV nanocomposite exhibits highly efficient thermocatalytic activities toward selective nitro reduction employing HCOONH<sub>4</sub> as a hydrogen source under ambient conditions. Controlled experiments demonstrate that the •CO<sub>2</sub><sup>–</sup> radicals formed by the dehydrogenation of the HCOONH<sub>4</sub> are the main active species for the nitro compounds reduction. The underlying mechanism for such a room temperature thermocatalytic reduction of nitro compounds is discussed accordingly. In addition, defective TiO<sub>2</sub> nanostructures deposited with Pd nanoparticles, featuring excellent visible light absorption via the creation of oxygen vacancies, can also utilize thermal energy along with solar energy to drive catalytic reduction reactions more efficiently at room temperature. During this process, the oxygen vacancies and Pd nanoparticles play synergetic roles in the photo-reduction of nitro compounds. Our promising results may offer useful information for the design of novel defect-mediated catalytic system which couples solar light energy with thermal energy to drive an energy efficient catalytic process.

## 2. EXPERIMENTAL SECTION

**2.1. Materials.** Trifluorotoluene (BTF) with a purity of >99% and active carbon (>99%) were supplied by Alfa Aesar. Degussa P25 was supplied from Degussa, Huls Corporation, Germany. 5,5-Dimethyl-1-

pyrroline *N*-oxide (DMPO) with a purity of >97% was purchased from Sigma-Aldrich. Palladium(II) chloride (PdCl<sub>2</sub>), polyvinylpyrrolidone (PVP), sodium borohydride (NaBH<sub>4</sub>) anhydrous ethanol (>99%), benzyl alcohol (>99%) (BA), hydrochloric acid (HCl), ammonium formate (HCOONH<sub>4</sub>), 2-nitroaniline (C<sub>6</sub>H<sub>6</sub>N<sub>2</sub>O<sub>2</sub>), 3-nitroaniline (C<sub>6</sub>H<sub>6</sub>N<sub>2</sub>O<sub>2</sub>), 4-nitroaniline (C<sub>6</sub>H<sub>6</sub>N<sub>2</sub>O<sub>2</sub>), 2-nitrophenol (C<sub>6</sub>H<sub>5</sub>NO<sub>3</sub>), 3-nitrophenol (C<sub>6</sub>H<sub>5</sub>NO<sub>3</sub>), 4-nitrophenol (C<sub>6</sub>H<sub>5</sub>NO<sub>3</sub>), 4-nitrotoluene (C<sub>7</sub>H<sub>7</sub>NO<sub>2</sub>) and 4-nitroanisole (C<sub>7</sub>H<sub>7</sub>NO<sub>3</sub>) were obtained from Sinopharm chemical reagent Co., Ltd. (Shanghai, China). Distilled water and ultrapure water were supplied from local sources. All the reagents were used without further purification.

**2.2. Synthesis.** (I) Preparation of P25 with oxygen vacancies. P25 with oxygen vacancies (P25-OV) was synthesized via a photocatalytic approach as reported previously.<sup>40,41</sup> Typically, 0.05 g of Degussa P25 was added into 3 mL of trifluorotoluene, which contained 0.4 mmol benzyl alcohol in a Pyrex glass bottle. Then the suspension was irradiated by a 300 W Xe arc lamp (PLS-SXE 300, Beijing Perfectlight Co. Ltd.) equipped with band-pass filter (365 ± 15 nm) for a 2 h photocatalytic reaction. After photo-oxidation, the residual P25-OV was extracted by centrifuge and rinsed with water and ethanol for several times. (II) Preparation of supported Pd–P25-OV composite. For the preparation of the H<sub>2</sub>PdCl<sub>4</sub> solution, a given amount of PdCl<sub>2</sub> powder was dissolved in the HCl solution. The as-obtained H<sub>2</sub>PdCl<sub>4</sub> solution has a concentration of 10 mM. The growth of Pd nanoparticles on P25-OV was performed as follows: 0.05 g of P25-OV was dispersed in 30 mL of distilled water under ultrasonication. Then 0.564 mL of 10 mM H<sub>2</sub>PdCl<sub>4</sub> solution was mixed with the P25-OV suspension under strong stirring. Then the suspension was transferred into a round-bottom flask and was heated to 100 °C in an oil bath under vigorous stirring for 2 h. Then the resulting Pd–P25-OV was cooled down and collected, rinsed with ethanol and water and then dried at 60 °C overnight. For the purpose of comparison, the colloidal Pd nanoparticles supported on the P25-OV were also prepared. For details, please see the Supporting Information.

**2.3. Characterization.** The crystal structures of the catalysts were characterized by a Bruker D8 Advance X-ray diffractometer (XRD) with Cu K $\alpha$  radiation. The optical properties of the catalysts were investigated by a Cary 500 UV–visible ultraviolet/visible diffuse reflectance spectrophotometer (DRS), during which BaSO<sub>4</sub> was utilized as the internal reflectance standard. The morphology of the resulting samples was investigated by a transmission electron microscopy (TEM, FEI Tecnai G2 F20 S-TWIN). X-ray photoelectron spectroscopy (XPS) analysis was conducted using a Thermo Scientific ESCA Lab250 spectrometer, which consists of a monochromatic Al K $\alpha$  as the X-ray source a hemispherical analyzer and sample stage with multiaxial adjustability to obtain the composition on the surface of samples. All the binding energies were calibrated by the C 1s peak of the surface adventitious carbon at 284.6 eV. Electron spin resonance (ESR) analysis of oxygen vacancy was operated at a Bruker EPR A300 spectrometer. Typically, a 0.1 g sample powder was put into a quartz–glass sample tube. Then the sample was analyzed by the ESR instrument under room temperature. The settings for the ESR spectrometer were the following: modulation frequency, 100.00 kHz; center field, 3580.26 G; power, 6.34 mW; microwave frequency, 9.50 GHz. ESR signal of the radicals spin-trapped by 5,5-dimethyl-1-pyrroline-*N*-oxide (DMPO) was also recorded on a Bruker EPR A300 spectrometer at room temperature. General instrument setting were as follows: microwave power, 6.35 mW; modulation amplitude, 3 G; receiver gain, 1 × 10<sup>3</sup>; time constant, 10.24 ms; sweep time, 42 s; center field, 3507 G; sweep width, 80 G. The DMPO–•CO<sub>2</sub><sup>–</sup> adduct was generated from a sample Pd–P25-OV aqueous suspension (20 mg of sample dispersed in 0.5 mL of ultrapure water) in the presence of 5 mg of HCOONH<sub>4</sub> and 15 mM DMPO in the dark at room temperature. Before the experiment, the ultrapure water was further purified by active carbon. The photoluminescence spectra for the samples were recorded on an Edinburgh FL/FS900 spectrophotometer, and the excitation wavelength was set at 365 nm.

**2.4. Activity.** **2.4.1. Thermocatalytic Activity.** The catalytic nitro reduction was conducted as follows. Ten milligrams of catalyst powder was dispersed into 40 mL of the aqueous nitro solution (10 mg·L<sup>–1</sup>) in

a quartz vial. Then the reaction solution was stirred in the dark for 1 h to make sure the establishment of an adsorption–desorption equilibrium between the catalyst and nitro compound. Then 40 mg of  $\text{HCOONH}_4$  was poured into the reaction solution. As the reactions proceed, 3 mL of the suspension was taken at a certain time interval and was centrifuged to remove the catalyst. Then the reaction solution was analyzed on a Varian UV–vis spectrophotometer (Cary-50, Varian Co.). The whole catalytic reaction was carried out under  $\text{N}_2$  bubbling at the flow rate of 60 mL/min. To determine the conversion and selectivity of the reaction, the reaction solution was analyzed with a Shimadzu High Performance Liquid Chromatograph (HPLC–LC20AT equipped with a C18 column and SPD-M20A photo diode array detector). Conversion and selectivity for reduction of nitro compounds were defined as the following:

$$\text{conversion (\%)} = [(C_0 - C_r)/C_0] \times 100$$

$$\text{selectivity (\%)} = [C_p/(C_0 - C_r)] \times 100$$

Where  $C_0$  is the initial concentration of nitro compound and  $C_r$  and  $C_p$  are the concentration of reactant nitro compound and product amine, respectively, at a certain time after the catalytic reaction.

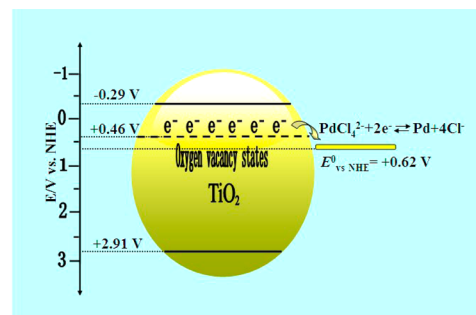
**2.4.2. Photocatalytic Activity.** As for the photoassisted nitro reduction in water, 10 mg of catalyst powder was dispersed into 80 mL of the aqueous nitro solution ( $20 \text{ mg}\cdot\text{L}^{-1}$ ) in a quartz vial. The reaction solution was stirred in the dark for 1 h to make sure the establishment of an adsorption–desorption equilibrium between the catalyst and aromatic nitro compounds. Then 40 mg of  $\text{HCOONH}_4$  was poured into the reaction solution. Meanwhile, the reaction system was irradiated by a 300 W Xe arc lamp (PLS-SXE 300, Beijing Perfectlight Co. Ltd.) with a UV-CUT filter ( $>420 \text{ nm}$ ). The reaction temperature was controlled at room temperature by an air-cooling system. As the reactions proceeded, 3 mL of the suspension was taken at a certain time interval and was centrifuged to remove the catalyst. Afterward, the solution was analyzed on a Varian UV–vis spectrophotometer (Cary-50, Varian Co.). The whole catalytic reaction was carried out under  $\text{N}_2$  bubbling at the flow rate of 60 mL/min. To determine the conversion and selectivity of the reaction, the reaction solution was analyzed with a Shimadzu High Performance Liquid Chromatograph, which is the same as that for thermocatalytic reduction nitro compounds.

### 3. RESULTS AND DISCUSSION

**3.1. Synthesis and Characterization.** With a novel defect-mediated reduction process developed in our lab,<sup>41</sup> the defective  $\text{TiO}_2$  (P25) with oxygen vacancies ( $\text{TiO}_2\text{-OV}$ ) is able to reduce the Pd (II) ions to metallic Pd nanoparticles on  $\text{TiO}_2\text{-OV}$ , as shown in Scheme 1. In this method, the commercially available Degussa P25 with oxygen vacancies (P25-OV) is first formed via a photocatalytic reaction with benzyl alcohol.<sup>41</sup> The as-synthesized P25-OV and metal salt ( $\text{H}_2\text{PdCl}_4$ ) are then mixed in aqueous solution. Upon the refluxing process, the metal ions are reduced by electrons trapped on the oxygen vacancy states (Scheme 1) and thus Pd nanoparticles are directly grown on the surface of defective P25-OV. Meanwhile, the P25-OV is partially oxidized by the Pd ions, as evidenced by the decreased ESR signal intensity at  $g = 2.004$  of Pd–P25-OV (Figure S1, Supporting Information).<sup>41</sup>

Notably, this defect-mediated reduction strategy can also be used to deposit Au, Pt and Ag nanoparticles on the defective P25-OV, as demonstrated previously.<sup>41,42</sup> However, among these noble metal nanoparticles, only Pd nanoparticles supported on P25-OV are active for selective nitro reduction in the presence of  $\text{HCOONH}_4$  under ambient conditions. In contrast, the Au, Pt and Ag nanoparticles are all silent under identical reaction conditions. Therefore, we herein are focused on investigation of Pd–P25-OV for catalytic nitro reduction,

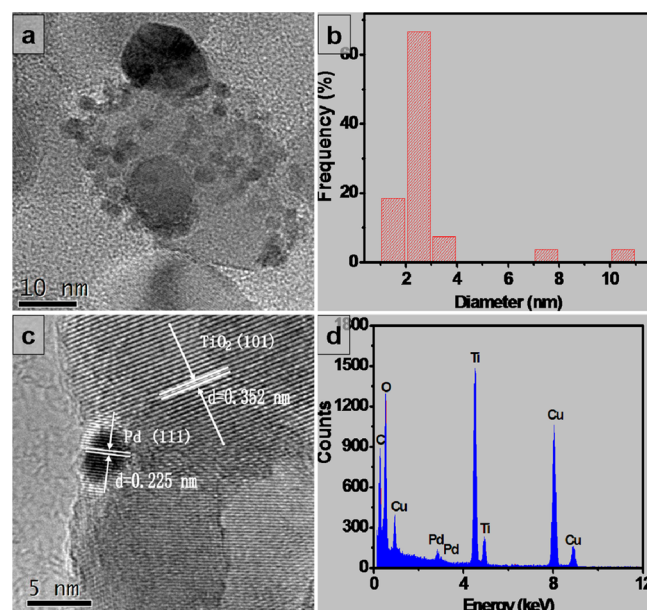
### Scheme 1. Proposed Mechanism of Defect-Mediated Reduction of Pd (II) Ions over the P25 with Oxygen Vacancies (P25-OV)<sup>a</sup>



<sup>a</sup>The reduction potential of the oxygen vacancy states is about 0.46 V vs NHE (normal hydrogen electrode), which is lower than that of  $\text{H}_2\text{PdCl}_4$  (0.62 V). The relative potential levels rationalize the thermodynamic feasibility of electron transfer from the oxygen vacancy states to the Pd(II) ions, leading to the reduction of the adsorbed Pd ions and formation of metallic Pd supported on P25-OV.

aiming to reveal the underlying mechanism of nitro reduction catalyzed by Pd–P25-OV.

Figure 1a shows a typical TEM image of a Pd–P25-OV catalyst, from which it is shown that Pd nanoparticles with an



**Figure 1.** Typical TEM image of Pd–P25-OV (a); size distribution plot of Pd nanoparticles (b); HRTEM image of Pd–P25-OV (c); EDX image of Pd–P25-OV (d).

average size of ca. 2 nm (Figure 1b) are highly dispersed on the defective P25-OV. The high-resolution TEM (HRTEM) analysis, as shown in Figure 1c, reveals the highly crystalline feature of the P25 and Pd nanoparticles. The fringes with lattice spacing of 0.352 nm and 0.225 nm could be assigned to the (101) facet of anatase  $\text{TiO}_2$  and (111) facet of face-centered cubic (fcc) Pd, respectively.<sup>35</sup> The energy-dispersive spectroscopy (EDS) analysis in Figure 1d confirms that the sample contains Ti, O and Pd elements. From the XRD analysis (Figure S2, Supporting Information), it is seen that the as-prepared samples are the mix phase of anatase and rutile of



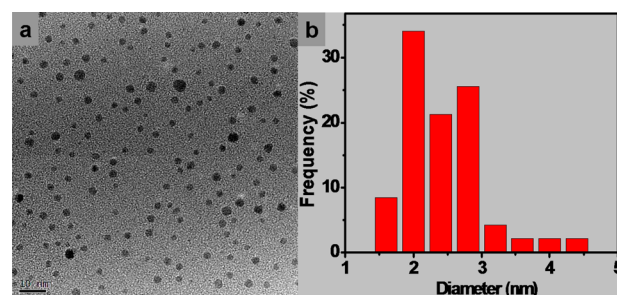
TiO<sub>2</sub>. Besides the peaks of TiO<sub>2</sub>, no other peaks are present, implying the uniform distribution and low weight loading of metal particles on the defective P25-OV.<sup>41</sup> The as-synthesized Pd–P25-OV sample can be easily dispersed in aqueous and organic solvents for potential catalytic applications (Figure S3, Supporting Information).

To confirm the Pd valence states, the X-ray photoelectron spectroscopy (XPS) analysis is conducted. The full XPS spectrum of Pd–P25-OV is shown in Figure S4a (Supporting Information). C, Pd, Ti and O elements are clearly observed, with characteristic peaks at binding energies of 285 (C 1s), 335 (Pd 3d), 459 (Ti 2p) and 530 eV (O 1s). Characteristic peaks at 334.6 and 339.9 eV in the Pd 3d spectrum (Figure S4b, Supporting Information) can be ascribed to the binding energies (BE) of Pd 3d<sub>5/2</sub> and Pd 3d<sub>3/2</sub> of metallic Pd<sup>0</sup>.<sup>43</sup> Therefore, the results of TEM, EDX and XPS analysis together confirm that the metallic Pd nanoparticles are successfully deposited on the P25-OV surface. The weight content of Pd estimated by XPS analysis is ca. 2.0 wt % in Pd–P25-OV. Taking the bulk Pd as a benchmark, it is found that Pd–P25-OV exhibits a Pd 3d<sub>5/2</sub> BE (334.6 eV), which is 0.7 eV lower than bulk Pd (335.3 eV).<sup>27</sup> This result suggests that a partial negative charge metal phase (Pd<sup>δ-</sup>) is formed, which is resulted from a strong metal-support interaction.<sup>41,42</sup> This is due to the fact that the oxygen vacancies on P25-OV can stabilize the Pd nanoparticles.<sup>41</sup> These results demonstrate that our preparation method not only presents a simple yet efficient method to fabricate small sized Pd nanoparticles without foreign reducing agents but also offers a feasible way to modify the electronic properties of supported metal nanoparticles.

**3.2. Catalytic Reduction of Aromatic Nitro Compounds.** Initially, 4-nitroaniline (4-NA) is used as a model aromatic nitro compound to investigate the catalytic activity of Pd–P25-OV in the presence of HCOONH<sub>4</sub> under ambient conditions. A controlled experiment shows that the nitro reduction does not occurred even with a large amount of HCOONH<sub>4</sub> without the Pd–P25-OV catalyst. Furthermore, the Au, Ag and Pt–P25-OV catalysts,<sup>41,42</sup> which are prepared using the same method as Pd–P25-OV, are all not active for this reaction. However, in contrast, it is impressive to find that Pd–P25-OV is active under identical reaction conditions. As shown in Figure S5 (Supporting Information), the absorption peak of 4-NA is rapidly decreased and two peaks at 238 and 305 nm simultaneously appeared in the presence of Pd–P25-OV. These two peaks can be attributed to the characteristic peaks of *p*-phenylenediamine (PPD),<sup>44</sup> indicating the reduction of 4-NA to PPD by the Pd–P25-OV catalyst. The high performance liquid chromatograph (HPLC) analysis further indicates that 4-NA is reduced to PPD with a high selectivity (ca. 99%). Notably, the reduction reaction could not proceed without the N<sub>2</sub> purge (Figure S6, Supporting Information), as it is essential to provide an anaerobic atmosphere to avoid the reoxidation of the reduction product (PPD). In addition, the Pd–P25-OV in the absence of HCOONH<sub>4</sub> gives no conversion of 4-NA, which is observed under the same reaction conditions (Figure S6, Supporting Information), indicating that ammonium formate is necessary to drive the reduction process. Besides, it is worth noting that the reduction reaction over Pd–P25-OV starts instantaneously after the addition of HCOONH<sub>4</sub>, and no induction time is needed. This would be advantageous for ease of use in real technological applications.

To demonstrate the catalytic advantage of our method for synthesis of Pd nanoparticles, we also have prepared the Pd

nanoparticles stabilized by PVP (Pd–PVP) with an average size of ca. 2 nm by a colloidal method (Figure 2).<sup>45</sup> Then, the Pd



**Figure 2.** TEM image of the as-prepared Pd nanoparticles stabilized by polyvinyl pyrrolidone (PVP) (a); the size distribution of Pd nanoparticles (b).

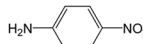
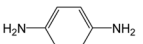
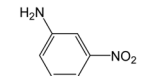
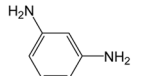
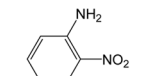
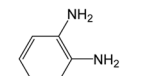

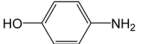
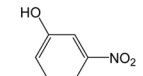
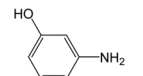
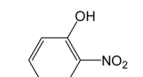
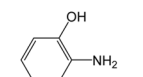
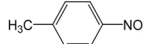
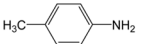
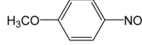
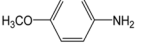
colloidal nanoparticles are loaded onto the supported P25-OV, by which the Pd/P25-OV–PVP catalyst is obtained. The catalytic activities of Pd–PVP and Pd/P25-OV–PVP are investigated under identical experimental conditions. The bare unsupported Pd–PVP nanoparticles show extremely low activity in the reduction of 4-NA, as shown in Figure S7 (Supporting Information). After deposition of Pd–PVP on the defective P25-OV, an enhanced activity toward 4-NA reduction is clearly observed (Figure S7, Supporting Information). However, the Pd/P25-OV–PVP possesses only very slight catalytic performance as compared to Pd–P25-OV (Figure S8, Supporting Information). Considering that the sizes of Pd nanoparticles in these catalysts are almost the same, the poor activity of the Pd/P25-OV–PVP is attributed to the presence of stabilizing organic ligands (PVP). This is due to the fact that they can strongly interact with the metal surface and hinder the access of reactant to the metal surface.<sup>33</sup>

To examine the efficacy of Pd–P25-OV, we have tested the thermocatalytic activities of Pd–P25-OV toward the reduction of various substituted aromatic nitro compounds under the same reaction conditions (Table 1). It is seen that Pd–P25-OV demonstrates remarkably improved activity as compared to Pd/P25-OV–PVP. The reduction reaction proceeds very fast over Pd–P25-OV, which is over within 6 minutes in most cases. Moreover, the reaction is highly selective for the production of a series of aromatic amines. These results illustrate the excellent generality and high selectivity of Pd–P25-OV catalyzed nitro reduction process at room temperature in water. Notably, in this heterogeneous catalyst system, ammonium formate also has the advantages of being a readily available, inexpensive, stable and nontoxic base. These factors largely improve the environmental and economical impact of this Pd-catalyzed hydrogenation reaction.

### 3.3. Mechanism of Thermocatalytic Nitro Reduction.

In terms of the reduction mechanism of nitro compounds, one may speculate that the defective P25-OV supported Pd nanoparticles catalyzed nitro reduction could be driven by the reductive oxygen vacancy states. However, this possibility can be excluded, because the reaction does not proceed when P25-OV (or P25) is used instead of Pd–P25-OV as the catalyst (Figure S9, Supporting Information). In fact, previous report on TiO<sub>2</sub> has also supported that the reductive sites (i.e., Ti<sup>3+</sup> and oxygen vacancies) are not active for the reduction of nitro compounds.<sup>46</sup> These results demonstrate that the nitro reduction is primarily driven by the Pd nanoparticles, in

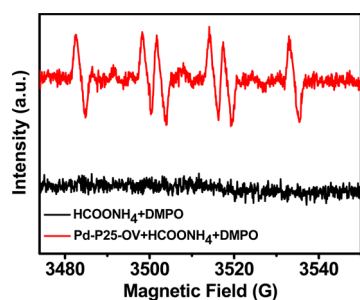
**Table 1. Thermocatalytic Reduction of Various Aromatic Nitro Compounds in Water over Pd–P25-OV for 6 min at Room Temperature<sup>a</sup>**

| Substrate   | Product   | Conversion (%) | Selectivity (%) |
|---|---|----------------|-----------------|
|  |  | 99 (8)         | 99 (98)         |
|  |  | 95 (10)        | 98 (97)         |
|  |  | 97 (15)        | 97 (97)         |
|  |  | 98 (14)        | 97 (96)         |
|  |  | 96 (19)        | 99 (98)         |
|  |  | 95 (20)        | 98 (99)         |
|  |  | 85 (26)        | 99 (98)         |
|  |  | 89 (25)        | 97 (99)         |

<sup>a</sup>The data in parentheses are conversion and selectivity over Pd/P25-OV–PVP under identical reaction conditions.

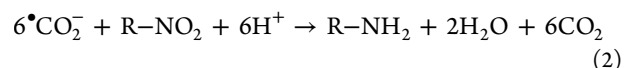
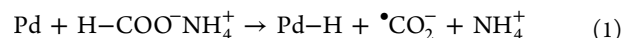
which the electron transfer from the HCOONH<sub>4</sub> to aromatic nitro compounds is mediated by Pd nanoparticles.

To understand the microscopic details of the Pd mediated electron transfer process, ESR analysis coupled with DMPO spin-trapping is conducted. As shown in Figure 3, sextet

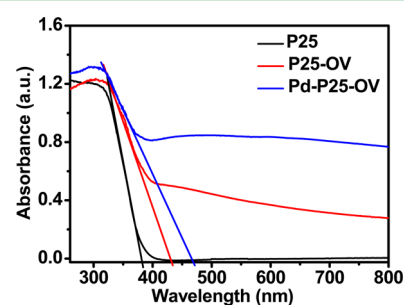
**Figure 3.** DMPO spin-trapping ESR spectra of the Pd–P25-OV in the presence of HCOONH<sub>4</sub> under ambient conditions.

characteristic peaks of the DMPO–<sup>•</sup>CO<sub>2</sub><sup>–</sup> adduct can be clearly observed only in the presence of Pd–P25-OV and HCOONH<sub>4</sub>.<sup>44</sup> No apparent signals are detected in the presence of P25-OV (or P25) and HCOONH<sub>4</sub>. The formation mechanism of <sup>•</sup>CO<sub>2</sub><sup>–</sup> radicals in the presence of HCOONH<sub>4</sub> has been investigated previously.<sup>47</sup> It is proposed that the dehydrogenation of the ammonium formate is responsible for the formation of <sup>•</sup>CO<sub>2</sub><sup>–</sup> radicals.<sup>47</sup> During this process, Pd nanoparticles are transferred to Pd–H by dehydrogenation of ammonium formate,<sup>39,47</sup> and consequently the <sup>•</sup>CO<sub>2</sub><sup>–</sup> radicals are formed. The <sup>•</sup>CO<sub>2</sub><sup>–</sup> radicals with strong reducing power ( $E_{(\text{CO}_2^{\bullet-}/\text{CO}_2^-)}^0 = -1.8 \text{ V}$ ) are proved to be highly active for nitro reduction.<sup>44</sup> In addition, as Pd–H is not stable, it would decompose during the catalytic reaction to generate Pd and

hydrogen for the hydrogenation of the nitro compounds.<sup>39,48</sup> Accordingly, we can express the nitro reduction mechanism catalyzed by supported Pd nanoparticles as the following elementary steps (1)–(3).



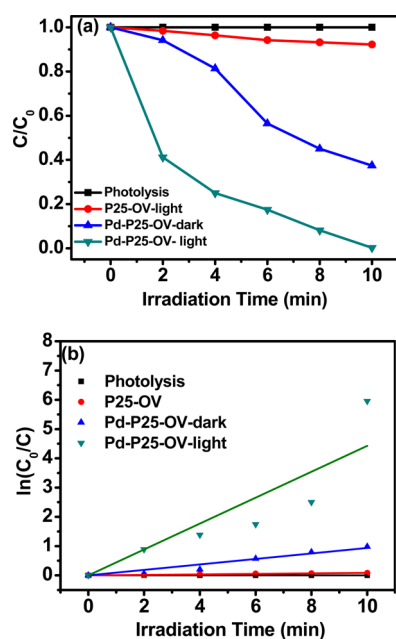
**3.4. Photoassisted Catalytic Reduction of Nitro Compounds.** Unlike the photoinactive support (carbon, MgO, SiO<sub>2</sub>), the photoactive semiconductor TiO<sub>2</sub> offers the possibility of light-enhanced catalytic reduction of nitro compounds.<sup>49,50</sup> In particular, the presence of oxygen vacancies narrows the band gap of TiO<sub>2</sub>, as shown in Figure 4, which

**Figure 4.** UV–vis diffuse reflectance spectra (DRS) of the P25, P25 with oxygen vacancies (P25-OV) and Pd–P25-OV.

allows P25-OV to absorb visible light. Therefore, measurements are performed with the use of a lamp emitting in the visible range (>420 nm). To test this hypothesis, we firstly examine the light effects of Pd–P25-OV on the catalytic reduction of 4-NA. Selected results are shown in Figure 5. In a control experiment in the presence of HCOONH<sub>4</sub> without catalyst, no positive influence of light is observed. Remarkably, in the presence of Pd–P25-OV and HCOONH<sub>4</sub>, a considerable accelerating effect of irradiation is seen. Although the photothermal effect could, in principle, contribute to the final conversion of the reduction product, the reaction temperature is kept constant to eliminate the influence of the thermal effect caused by light irradiation and thus investigates the photocatalytic nature of the reduction reaction.

To evaluate the catalytic efficiency of the photocatalyst, it is necessary to determine the turnover number (TON) and the turnover frequency (TOF) of the catalytic reaction. In heterogeneous catalysis, the TON is the number of the reactant molecules which are converted into the products while the weight content of the catalyst is 1 g, and the TOF is equal to the value of TON/time.<sup>44</sup> Therefore, the TON of the Pd–P25-OV with or without visible light irradiation is estimated to be  $1.7 \times 10^{20}$  and  $1.0 \times 10^{20}$  molecules·g<sup>–1</sup>, respectively. By analogy, the TOF of the Pd–P25-OV with or without visible light irradiation is determined to be  $2.9 \times 10^{17}$  and  $1.8 \times 10^{17}$  molecules·g<sup>–1</sup>·s<sup>–1</sup>, respectively.

To confirm the role of oxygen vacancies during photocatalytic process, controlled experiments using Pd/P25–PVP without oxygen vacancies are performed for photocatalytic 4-NA reduction. As shown in Figure S10 (Supporting Information), the Pd/P25–PVP shows almost no enhanced activity under the irradiation of visible light than that of the Pd/



**Figure 5.** Photocatalytic performance of the as-synthesized samples for selective reduction of 4-nitroaniline (4-NA) under ambient conditions (a); and the corresponding kinetic rate constant curve (b). Note: the amount of 4-NA used herein is 4 times that used in thermocatalytic reduction process of 4-NA.

Pd–PVP without light irradiation. This result indicates that the presence of oxygen vacancies is necessary for activating the wide-band-gap  $\text{TiO}_2$  under visible light irradiation. In addition, bare P25-OV as a contrast test gives only a very slight activity even under light irradiation, indicating that metal-semiconductor heteronanostructures are of key importance for driving the nitro reduction reaction. In addition, Au, Ag and Pt supported on the P25-OV<sup>41,42</sup> which are prepared using the same method as Pd–P25-OV, are also tested for the photocatalytic nitro reduction. Although these catalysts show enhanced photoactivities when compared with the bare P25-OV (Figure S11, Supporting Information), their activities are much lower than Pd–P25-OV. The obviously enhanced activity of Pd–P25-OV is attributed to the following two reasons. First, Pd nanoparticles with smaller particle size are much more favorable for photogenerated charge-carrier separation than that of noble metal nanoparticles (Au, Ag and Pt) with larger particle size (Table S1, Supporting Information), which has already been investigated previously.<sup>42</sup> Second, as compared with the other noble metal nanoparticles (Au, Ag and Pt), Pd nanoparticles supported on defective P25-OV are highly active for thermocatalytic reduction of 4-NA even at room temperature without light irradiation. Therefore, in the Pd–P25-OV catalytic system, thermal energy coupled with visible light energy can be effectively utilized to drive a more efficient catalytic process.

Moreover, it is worth noting that, because the visible light irradiation is able to significantly accelerate the photoreduction process of 4-NA, the used amount of 4-NA in photocatalytic reduction of 4-NA is remarkably increased to 4 times of that used in thermocatalytic reduction process of 4-NA. In this sense, the above results demonstrate clearly that the Pd–P25-OV nanostructure allows light energy to be efficiently utilized for remarkably accelerating the reduction of 4-NA. To examine its general applicability, the resulting Pd–P25-OV is also used

as catalyst for the hydrogenation of a series of nitroaromatics using  $\text{HCOONH}_4$  as a reducing agent (Table 2). It is shown

**Table 2. Photocatalytic Reduction of Various Aromatic Nitro Compounds in Water over Pd–P25-OV under Visible Light Irradiation ( $\lambda > 420$  nm) for 10 min at Room Temperature<sup>a</sup>**

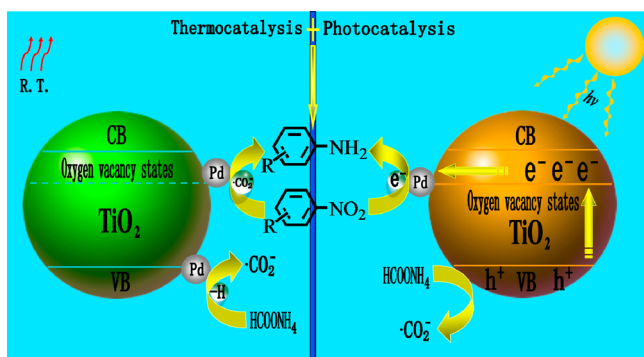
| Substrate | Product | Conversion (%) | Selectivity (%) |
|-----------|---------|----------------|-----------------|
|           |         | 99 (63)        | 99 (99)         |
|           |         | 99 (30)        | 97 (95)         |
|           |         | 97 (65)        | 98 (96)         |
|           |         | 88 (24)        | 99 (96)         |
|           |         | 99 (31)        | 98 (97)         |
|           |         | 95 (40)        | 99 (98)         |
|           |         | 80 (27)        | 99 (99)         |
|           |         | 88 (35)        | 96 (96)         |

<sup>a</sup>The data in parentheses are conversion and selectivity over Pd–P25-OV under identical reaction conditions without visible light irradiation.

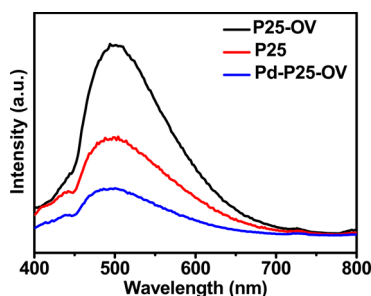
that the interaction of Pd–P25-OV catalyst with visible light results in a higher activity of Pd–P25-OV toward aromatic nitro reduction. Most of the substituted aromatic nitro compounds could undergo photocatalytic reduction to the corresponding amines with high yields within 10 minutes. These results illustrate such a Pd–P25-OV composite catalyst is able to couple solar light energy with the thermal energy to driven a more energy efficient catalytic process. The other issue that should be mentioned is about the stability of the oxygen vacancies during the photo- and thermocatalytic processes. Given this issue, ESR analysis is utilized to investigate the changes that occurred in the defect structure of Pd–P25-OV during the catalytic reactions. As shown in Figure S12 (Supporting Information), almost no changes of the oxygen vacancies concentration are observed on the Pd–P25-OV before and after thermo- and photocatalytic processes. These results indicate that the oxygen vacancies on Pd–P25-OV are stable during catalytic reactions.

On basis of the previous reports on photocatalytic reduction of nitro compounds, we propose the mechanism of catalytic nitro reduction over Pd–P25-OV under the irradiation of visible light, as schematically shown in Figure 6.<sup>5,6,15</sup> As irradiated by the visible light, the defective P25-OV is able to generate electron and hole pairs. Because the photogenerated holes can be captured by the  $\text{HCOONH}_4$ ,<sup>5,6,15</sup> the photogenerated electrons with strong reducing power can participate in the nitro reduction. For the bare P25-OV, the large amounts of oxygen vacancies serve as charge recombination centers, as revealed by the photoluminescence analysis (Figure 7). Therefore, the P25-OV shows very low photocatalytic activity toward nitro reduction. In the case of Pd–P25-OV, the





**Figure 6.** Schematic diagram of the proposed mechanism for photoassisted reduction of aromatic nitro compounds over the Pd-P25-OV nanocomposite under visible light irradiation ( $\lambda > 420$  nm).



**Figure 7.** Photoluminescence (PL) spectra of the P25, P25 with oxygen vacancies (P25-OV) and Pd-P25-OV. The influences of Pd deposition on the charge separation process are two-fold. Firstly, the Pd deposition can decrease the concentration of oxygen vacancies, the charge recombination sites, on the defective P25-OV, during the growth process. Secondly, the Pd nanoparticles can serve as electron sinks to promote the separation of the electron-hole pairs.

deposition of the Pd nanoparticles can effectively promote the photogenerated charge carriers separation process on photoexcited Pd-P25-OV (Figure 7), thereby enhancing the photoactivity of the P25-OV. As compared with the Pd-P25-OV without light irradiation, the nitro reduction mediated by photogenerated electrons provides an additional reaction pathway for amine production. During this process, the  $\cdot\text{CO}_2^-$  radicals and photogenerated electrons can directly take part in the hydrogenation of the nitro compounds to amines in water solution under  $\text{N}_2$  atmosphere. In addition, the photogenerated electrons trapped on the Pd nanoparticles would increase their electron density, favoring interaction with the electron deficient aromatic nitro compounds via an electrostatic force.<sup>31</sup> This is due to the fact that  $-\text{NO}_2$  function could result in electron deficient benzene ring and favor the interaction with electron rich Pd nanoparticles.<sup>27</sup> Moreover, the photogenerated holes can also react with the  $\text{HCOO}^-$  anions and generate the  $\cdot\text{CO}_2^-$  radicals with strong reducing power ( $E_{(\text{CO}_2^-/\cdot\text{CO}_2^-)}^0 = -1.8$  V), which has been demonstrated as the active species for nitro reduction.<sup>47</sup> Therefore, it is rationalized to observe enhanced activities for nitro reduction over Pd-P25-OV under visible light irradiation.

#### 4. CONCLUSION

In conclusion, Pd nanoparticles (ca. 2 nm) are uniformly deposited on the defective  $\text{TiO}_2$  with oxygen vacancies ( $\text{TiO}_2\text{-OV}$ ) by a defect mediated strategy. The resulting Pd- $\text{TiO}_2\text{-OV}$  shows highly thermocatalytic activities for the selective nitro

reduction using  $\text{HCOONH}_4$  as the reducing agent under ambient conditions. It is demonstrated that the thermoreduction of nitroaromatics is primarily driven by Pd nanoparticles. In addition, visible light energy is also utilized for accelerating the nitro reduction process, in which the oxygen vacancies and Pd nanoparticles play synergistic roles in the photoreduction of nitro compounds. It is hoped that our work would be beneficial for the development of novel defect-mediated catalytic system that solar light energy can be coupled with thermal energy to effectively drive chemical conversion under mild conditions.

#### ■ ASSOCIATED CONTENT

##### Supporting Information

Additional experimental details, characterizations, and data for thermocatalytic and photocatalytic reactions. This material is available free of charge via the Internet at <http://pubs.acs.org>.

#### ■ AUTHOR INFORMATION

##### Corresponding Author

\*Prof. Yi-Jun Xu. E-mail: [yjxu@fzu.edu.cn](mailto:yjxu@fzu.edu.cn). Tel.: +86 591 83779326.

##### Notes

The authors declare no competing financial interest.

#### ■ ACKNOWLEDGMENTS

The support by the National Natural Science Foundation of China (21173045, 20903023), the Award Program for Minjiang Scholar Professorship, the Natural Science Foundation (NSF) of Fujian Province for Distinguished Young Investigator Grant (2012J06003), Program for Returned High-level Overseas Chinese Scholars of Fujian province, and the Project Sponsored by the Scientific Research Foundation for the Returned Overseas Chinese Scholars, State Education Ministry, is gratefully acknowledged.

#### ■ REFERENCES

- (1) Samec, J. S. M.; Backvall, J.-E.; Andersson, P. G.; Brandt, P. *Chem. Soc. Rev.* **2006**, *35*, 237–248.
- (2) Tafesh, A. M.; Weigun, J. *Chem. Rev.* **1996**, *96*, 2035–2052.
- (3) Nomura, K. *J. Mol. Catal. A: Chem.* **1998**, *130*, 1–28.
- (4) He, L.; Wang, L.-C.; Sun, H.; Ni, J.; Cao, Y.; He, H.-Y.; Fan, K.-N. *Angew. Chem., Int. Ed.* **2009**, *48*, 9538–9541.
- (5) Zhang, N.; Xu, Y.-J. *Chem. Mater.* **2013**, *25*, 1979–1988.
- (6) Zhang, Y.; Zhang, N.; Tang, Z.-R.; Xu, Y.-J. *ACS Sustainable Chem. Eng.* **2013**, *1*, 1258–1266.
- (7) Kantam, M. L.; Chakravarti, R.; Pal, U.; Sreedhar, B.; Bhargava, S. *Adv. Synth. Catal.* **2008**, *350*, 822–827.
- (8) Cai, S.; Duan, H.; Rong, H.; Wang, D.; Li, L.; He, W.; Li, Y. *ACS Catal.* **2013**, *3*, 608–612.
- (9) del Pozo, C.; Corma, A.; Iglesias, M.; Sánchez, F. *J. Catal.* **2012**, *291*, 110–116.
- (10) Lin, W.; Cheng, H.; Ming, J.; Yu, Y.; Zhao, F. *J. Catal.* **2012**, *291*, 149–154.
- (11) Meng, X.; Cheng, H.; Akiyama, Y.; Hao, Y.; Qiao, W.; Yu, Y.; Zhao, F.; Fujita, S.-i.; Arai, M. *J. Catal.* **2009**, *264*, 1–10.
- (12) Sarmah, P. P.; Dutta, D. K. *Green Chem.* **2012**, *14*, 1086–1093.
- (13) Baron, M.; Metay, E.; Lemaire, M.; Popowycz, F. *Green Chem.* **2013**, *15*, 1006–1015.
- (14) Chen, Z.; Liu, S.; Yang, M.-Q.; Xu, Y.-J. *ACS Appl. Mater. Interfaces* **2013**, *5*, 4309–4319.
- (15) Liu, S.; Chen, Z.; Zhang, N.; Tang, Z.-R.; Xu, Y.-J. *J. Phys. Chem. C* **2013**, *117*, 8251–8261.
- (16) Liu, L.; Gu, X.; Ji, Z.; Zou, W.; Tang, C.; Gao, F.; Dong, L. *J. Phys. Chem. C* **2013**, *117*, 18578–18587.

- (17) Schabel, T.; Belger, C.; Plietker, B. *Org. Lett.* **2013**, *15*, 2858–2861.
- (18) Chen, Y.; Qiu, J.; Wang, X.; Xiu, J. *J. Catal.* **2006**, *242*, 227–230.
- (19) Corma, A.; Concepción, P.; Serna, P. *Angew. Chem., Int. Ed.* **2007**, *119*, 7404–7407.
- (20) Corma, A.; Serna, P. *Science* **2006**, *313*, 332–334.
- (21) Haruta, M. *Nature* **2005**, *437*, 1098–1099.
- (22) Enache, D. I.; Edwards, J. K.; Landon, P.; Solsona-Espriu, B.; Carley, A. F.; Herzing, A. A.; Watanabe, M.; Kiely, C. J.; Knight, D. W.; Hutchings, G. J. *Science* **2006**, *311*, 362–365.
- (23) Shiraiishi, Y.; Togawa, Y.; Tsukamoto, D.; Tanaka, S.; Hirai, T. *ACS Catal.* **2012**, *2*, 2475–2481.
- (24) Mitsudome, T.; Mikami, Y.; Matoba, M.; Mizugaki, T.; Jitsukawa, K.; Kaneda, K. *Angew. Chem., Int. Ed.* **2012**, *51*, 136–139.
- (25) Xiao, F. *J. Phys. Chem. C* **2012**, *116*, 16487–16498.
- (26) Lou, X.-B.; He, L.; Qian, Y.; Liu, Y.-M.; Cao, Y.; Fan, K.-N. *Adv. Synth. Catal.* **2011**, *353*, 281–286.
- (27) Cárdenas-Lizana, F.; Hao, Y.; Crespo-Quesada, M.; Yuranov, I.; Wang, X.; Keane, M. A.; Kiwi-Minsker, L. *ACS Catal.* **2013**, *3*, 1386–1396.
- (28) Corma, A.; Serna, P.; Concepción, P.; Calvino, J. J. *J. Am. Chem. Soc.* **2008**, *130*, 8748–8753.
- (29) Kundu, S.; Wang, K.; Liang, H. *J. Phys. Chem. C* **2009**, *113*, 5157–5163.
- (30) Shimizu, K.-i.; Miyamoto, Y.; Satsuma, A. *J. Catal.* **2010**, *270*, 86–94.
- (31) Wang, X.; Perret, N.; Delgado, J. J.; Blanco, G.; Chen, X.; Olmos, C. M.; Bernal, S.; Keane, M. A. *J. Phys. Chem. C* **2012**, *117*, 994–1005.
- (32) Liao, F.; Huang, Y.; Ge, J.; Zheng, W.; Tedsree, K.; Collier, P.; Hong, X.; Tsang, S. C. *Angew. Chem., Int. Ed.* **2011**, *123*, 2210–2213.
- (33) Cozzoli, P. D.; Comparelli, R.; Fanizza, E.; Curri, M. L.; Agostiano, A.; Laub, D. *J. Am. Chem. Soc.* **2004**, *126*, 3868–3879.
- (34) Dong, S.; Chen, X.; Wang, S.; Gu, L.; Zhang, L.; Wang, X.; Zhou, X.; Liu, Z.; Han, P.; Duan, Y.; Xu, H.; Yao, J.; Zhang, C.; Zhang, K.; Cui, G.; Chen, L. *ChemSusChem* **2012**, *5*, 1712–1715.
- (35) Teranishi, T.; Miyake, M. *Chem. Mater.* **1998**, *10*, 594–600.
- (36) Lee, J.; Shim, H. S.; Lee, M.; Song, J. K.; Lee, D. *J. Phys. Chem. Lett.* **2011**, *2*, 2840–2845.
- (37) Lopez-Sanchez, J. A.; Dimitratos, N.; Hammond, C.; Brett, G. L.; Kesavan, L.; White, S.; Miedziak, P.; Tiruvalam, R.; Jenkins, R. L.; Carley, A. F.; Knight, D.; Kiely, C. J.; Hutchings, G. J. *Nat. Chem* **2011**, *3*, 551–556.
- (38) Narayanan, R.; El-Sayed, M. A. *J. Am. Chem. Soc.* **2003**, *125*, 8340–8347.
- (39) Nag, N. K. *J. Phys. Chem. B* **2001**, *105*, 5945–5949.
- (40) Pan, X.; Zhang, N.; Fu, X.; Xu, Y.-J. *Appl. Catal., A* **2013**, *453*, 181–187.
- (41) Pan, X.; Xu, Y.-J. *Appl. Catal., A* **2013**, *459*, 34–40.
- (42) Pan, X.; Xu, Y.-J. *J. Phys. Chem. C* **2013**, *117*, 17996–18005.
- (43) Chen, S.; Li, J.; Qian, K.; Xu, W.; Lu, Y.; Huang, W.; Yu, S. *Nano Res.* **2010**, *3*, 244–255.
- (44) Wu, W.; Liu, G.; Liang, S.; Chen, Y.; Shen, L.; Zheng, H.; Yuan, R.; Hou, Y.; Wu, L. *J. Catal.* **2012**, *290*, 13–17.
- (45) Zhang, N.; Liu, S.; Fu, X.; Xu, Y.-J. *J. Phys. Chem. C* **2011**, *115*, 22901–22909.
- (46) Su, J.; Zou, X.-X.; Li, G.-D.; Li, L.; Zhao, J.; Chen, J.-S. *Chem. Commun.* **2012**, *48*, 9032–9034.
- (47) Perissinotti, L. L.; Brusa, M. A.; Grela, M. A. *Langmuir* **2001**, *17*, 8422–8427.
- (48) Saha, A.; Ranu, B. *J. Org. Chem.* **2008**, *73*, 6867–6870.
- (49) Zhai, Q.; Xie, S.; Fan, W.; Zhang, Q.; Wang, Y.; Deng, W.; Wang, Y. *Angew. Chem., Int. Ed.* **2013**, *125*, 5888–5891.
- (50) Chen, X.; Liu, L.; Yu, P. Y.; Mao, S. S. *Science* **2011**, *331*, 746–750.